



# Integrated spectral and image analysis of hyperspectral scattering data for prediction of apple fruit firmness and soluble solids content

Fernando Mendoza<sup>a,\*</sup>, Renfu Lu<sup>a</sup>, Diwan Ariana<sup>b</sup>, Haiyan Cen<sup>b</sup>, Benjamin Bailey<sup>a</sup>

<sup>a</sup> USDA/ARS, 105A/224 Farrall Hall, Michigan State University, East Lansing, MI 48824, USA

<sup>b</sup> Department of Biosystems and Agricultural Engineering, Michigan State University, East Lansing, MI 48824, USA

## ARTICLE INFO

### Article history:

Received 22 July 2010

Accepted 28 May 2011

### Keywords:

Apples

Firmness

Soluble solids

Hyperspectral imaging

Scattering profile analysis

Image analysis

## ABSTRACT

Spectral scattering is useful for assessing the firmness and soluble solids content (SSC) of apples. In previous research, mean reflectance extracted from the hyperspectral scattering profiles was used for this purpose since the method is simple and fast, and also gives relatively good predictions. The objective of this study was to improve firmness and SSC prediction for 'Golden Delicious' (GD), 'Jonagold' (JG), and 'Delicious' (RD) apples by integration of critical spectral and image features extracted from the hyperspectral scattering images over the wavelength region of 500–1000 nm, using spectral scattering profile and image analysis techniques. Scattering profile analysis was based on mean reflectance method and discrete and continuous wavelet transform decomposition, while image analysis included textural features based on first order statistics, Fourier analysis, co-occurrence matrix and variogram analysis, as well as multi-resolution image features obtained from discrete and continuous wavelet analysis. A total of 294 parameters were extracted by these methods from each apple, which were then selected and combined for predicting fruit firmness and SSC using partial least squares (PLS) method. Prediction models integrating spectral scattering and image characteristics significantly improved firmness and SSC prediction results compared with the mean reflectance method when used alone. The standard errors of prediction (SEP) for GD, JG, and RD apples were reduced by 6.6, 16.1, 13.7% for firmness ( $R_{pred}$ -values of 0.87, 0.95, and 0.84 and the SEPs of 5.9, 7.1, and 8.7 N), and by 11.2, 2.8, and 3.0% for SSC ( $R_{pred}$ -values of 0.88, 0.78, and 0.66 and the SEPs of 0.7, 0.7, and 0.9%), respectively. Hence, integration of spectral and image analysis methods provides an effective means for improving hyperspectral scattering prediction of fruit internal quality.

Published by Elsevier B.V.

## 1. Introduction

Firmness and soluble solids content (SSC) are important quality attributes that directly influence the consumer purchasing decision on fresh apple fruit (Lu, 2004). They are also important parameters in assessing apple maturity to determine optimal harvest dates (Qing et al., 2007). Currently, fruit maturity determination requires measuring multiple parameters including skin and flesh color, fruit firmness, sugar (or soluble solids content), starch pattern index, titratable acid, and ethylene production (Kingston, 1992). Standard methods for these quality measurements are mostly destructive, inefficient or time consuming, and prone to operational error. Hence, nondestructive sensing of fruit internal quality, especially firmness and SSC, is of great value in determining optimal harvest

time and ensuring high quality, consistent fruit for the consumer (Lu, 2004; Qing et al., 2007).

Researchers have explored different methods (i.e., mechanical, sonic, optical and electrical) for nondestructive evaluation of fruit quality. Among them is light scattering method, which has demonstrated great potential for assessing fruit firmness and SSC (Lu et al., 2009). The technique is based on the principle that scattering and absorption takes place when light interacts with the fruit tissue – scattering is largely influenced by density, tissue composition, particle size and cellular structures, whereas absorption is more closely associated with the chemical composition of the fruit (Birth, 1976). Hence appropriate quantification of light scattering features may enable us to better predict structurally related properties such as fruit firmness.

Earlier studies on light scattering technique used color CCD camera (Cho and Han, 1999; Tu et al., 1995) or single channel CCD detector (McGlone et al., 1997), coupled with laser(s), to quantify light scattering features for prediction of fruit firmness and/or ripeness. However, it is currently well known that scattering analysis at single wavelengths is not sufficient to predict fruit firmness

\* Corresponding author. Tel.: +1 517 432 7438; fax: +1 517 432 2892.

E-mail addresses: [fernando.mendoza@ars.usda.edu](mailto:fernando.mendoza@ars.usda.edu), [fmendoza@msu.edu](mailto:fmendoza@msu.edu) (F. Mendoza).

accurately (Lu, 2004). Hence recent research has been focused on multi- and/or hyper-spectral scattering technique (Lu, 2003, 2004, 2007; Lu and Peng, 2006, 2007; Peng and Lu, 2005, 2006, 2008; Lu et al., 2009). With this technique, a small continuous-wave light beam is incident on the fruit, generating diffusely reflected images at its surface around the incident point as a result of light propagation and backscattering inside the fruit. A multi- or hyper-spectral imaging system is used to capture backscattering images from the fruit at selected wavelengths or over a specific spectral region (e.g., 500–1000 nm). Spectral scattering features are extracted from the scattering images, and they are then applied to predict fruit firmness and SSC using an appropriate chemometric method.

While it is critical to develop a proper imaging system for accurate acquisition of spectral scattering images, it is equally important to apply appropriate mathematical methods for describing the spectral scattering features. Peng and Lu (2005) proposed a modified Lorentzian function for describing multispectral scattering profiles and its function parameters correlated well with the firmness of apples. In analyzing the hyperspectral scattering features to predict apple fruit firmness and SSC, Lu (2007) showed that a simple method of calculating mean reflectance for a specific scattering distance yielded good prediction results for fruit firmness and SSC when a neural network was used in the development of calibration models. Although these mathematical methods have shown great utility in describing the spectral scattering features, their relative performance in predicting fruit firmness and SSC is not quite clear because they were tested in separate studies, where the samples used were different and the experimental setups were not the same. Therefore, direct comparison of these mathematical methods is needed to determine which method is the most appropriate for predicting fruit firmness and SSC. Moreover, previous mathematical models are based on the analysis of individual or averaged spectral scattering profiles in the spectral dimension only, and they did not consider the pixel intensity distribution (also known as organization or intensity pattern) from the overall 2-D scattering images. The approach of analyzing 2-D scattering image features, coupled with 1-D spectral scattering profile analysis, could present an opportunity to improve quality prediction of apples.

The evaluation of texture features is important for image processing applications (Mendoza et al., 2007). Image texture can be defined as the spatial organization of intensity variations in an image at various wavelengths in the visible and short-wave near-infrared region. The spatial and spectral patterns of a hyperspectral scattering image acquired from each apple are related to, or reflect, the internal characteristics of the fruit (i.e., microstructure and chemical composition). Hence each hyperspectral scattering image would provide unique 2-D spectral and spatial scattering features or signatures for an apple fruit. Thus by analyzing the scattering images using image texture parameters which provide summary information about the local variation and pattern organization of the pixel intensity values on the image, researchers may ascertain or quantify some critical structural and chemical changes or features in apples that are related to fruit firmness and SSC.

The objective of this study was therefore to improve the prediction of firmness and SSC of 'Golden Delicious' (GD), 'Jonagold' (JG), and 'Delicious' (RD) apples by integration of critical information extracted from the hyperspectral scattering images based on 1-D scattering profiles and 2-D image analysis techniques. To better assess the performance of the proposed mathematical approach, scattering images for the wavelength region of 500–1000 nm were taken for three apple cultivars from two harvest seasons using two different hyperspectral imaging setups: a stationary system for GD in 2006 and a prototype on-line system for JG and RD in 2009.

## 2. Materials and methods

### 2.1. Apple samples

GD apples harvested in 2006 and JG and RD apples harvested in 2009 from the orchards of Michigan State University's Horticultural Teaching and Research Center in Holt, MI and Clarksville Horticultural Experiment Station in Clarksville, MI were used in this research. Different sample preparation procedures were used for apples harvested in 2006 and 2009.

For the 2006 experiment, GD apples were stored after harvest in a controlled atmosphere environment (2% O<sub>2</sub> and 3% CO<sub>2</sub> at 0 °C) for about five months. Imaging and reference firmness and SSC measurements were performed after the apples had been kept at room temperature (~24 °C) for at least 16 h. The experiment lasted six weeks for a total of 600 apples.

In 2009, JG and RD apples were harvested each week for six consecutive weeks in order to have a wider range of physiological conditions. One day after each harvest, a set of 100 apples for each cultivar were tested, and the rest apples were stored at 0 °C in refrigerated air. One week after the last harvest, tests for the stored apples were started. These apples were tested once a week for the first six weeks and then every two weeks for up to eight weeks. The experiment was completed in five months with a total of 928 JG apples and 1191 RD apples. The purpose of conducting the experiment over a five-month period was to have a large range of firmness distribution among the test apples. Similar to the 2006 experiment, the apples were kept at room temperature (~24 °C) for at least 16 h before the test was started.

### 2.2. Hyperspectral imaging systems

To evaluate and compare the performance and consistency of different mathematical methods proposed in this study, scattering images were acquired using two different hyperspectral imaging systems: a stationary hyperspectral imaging system and a prototype on-line hyperspectral imaging system (Fig. 1).

#### 2.2.1. Stationary hyperspectral imaging system (SHIS)

SHIS (Fig. 1a) was used for acquiring spectral scattering images from GD apples in 2006. This system mainly consisted of a high performance 512 × 512 pixel CCD camera (Model C4880-21-24A, Hamamatsu Photonics Systems, Bridgewater, New Jersey, USA), an imaging spectrograph (ImSpector V10, Spectral Imaging Ltd., Oulu, Finland) covering the wavelength region from 400 to 1000 nm, a quartz tungsten light halogen lamp (Oriel Instruments, Stratford, CT, USA) which was controlled by a DC power supply coupled with a light intensity controller, and a sample handling unit for automatically positioning each apple sample (to maintain the same surface height for apples of different sizes) for imaging. The fruit was illuminated by a steady-state light beam of 1.0 mm diameter at 15° with respect to the vertical axis and the line scanning position of the camera was set 1.5 mm off from the beam incident center to avoid saturation caused by high intensity signals. The acquisition of spatially resolved scattering images was carried out in line scanning mode as the fruit was moving on a motorized precision stage at a distance increment of 1 mm. The imaging unit line scanned the equatorial area of each fruit to capture reflectance (or scattering) images generated by the light source at the surface of the fruit. A total of 10 scattering images were acquired and they were then averaged to obtain one average scattering image. The SHIS was set to record scattering images with 256 × 256 pixel size after 2 × 2 binning, and the images acquired had spectral and spatial resolutions of 4.54 nm/pixel and 0.20 mm/pixel, respectively. The nonuniform instrument response of the system was tested on a white Teflon disk by following the procedure described in Qin and Lu (2007), and sub-

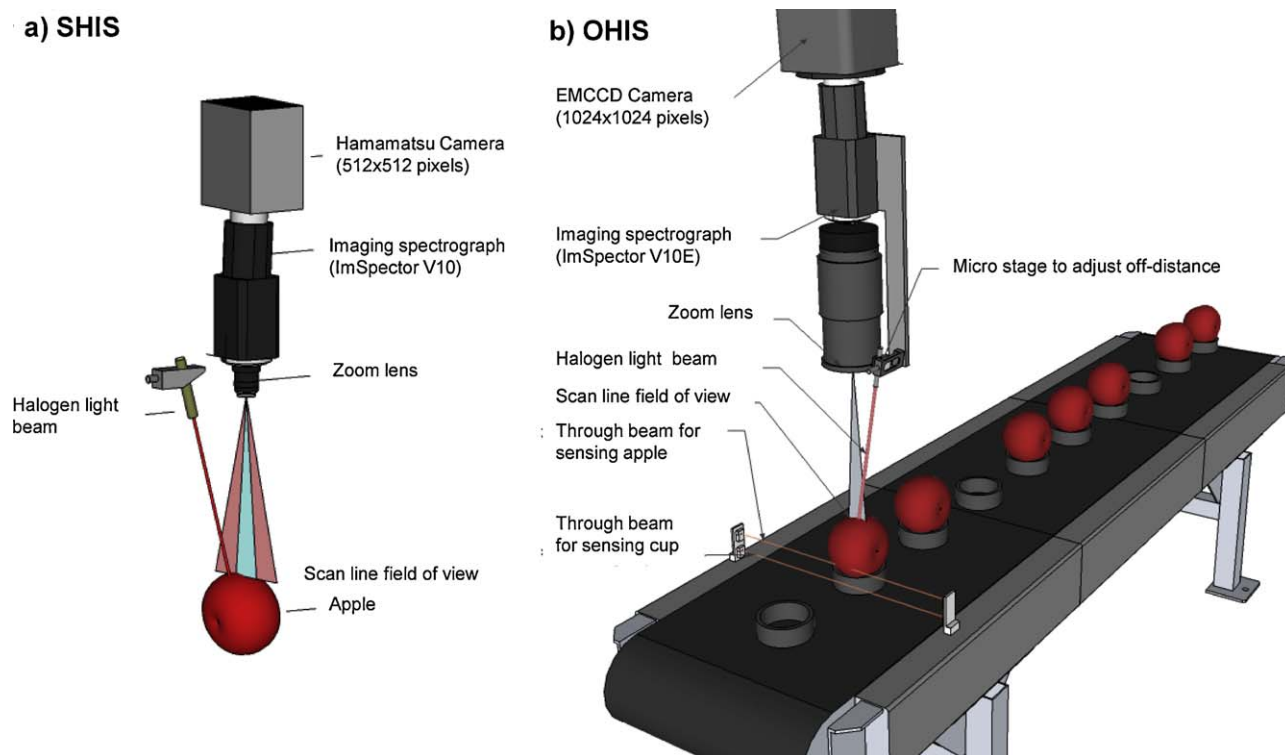


**Fig. 1.** Hyperspectral imaging systems for acquiring spectral scattering images from apple samples: (a) stationary system for evaluation of GD apples; (b) laboratory on-line system using an EMCCD for evaluation of JG and RD apples.

sequent corrections to the original reflectance profiles were made. A detailed description of the SHIS and the experimental setup is given in [Qin and Lu \(2008\)](#).

### 2.2.2. Prototype online hyperspectral imaging system (OHIS)

A laboratory OHIS ([Fig. 1b](#)) was used for acquiring spectral scattering images from JG and RD apples in 2009. This real-time system was similar to the one developed by [Lu and Peng \(2007\)](#) except that a hyperspectral imaging system was used in the current system, instead of a multispectral imaging configuration used in that study.

The prototype consisted of a back-illuminated electron-multiplying CCD (EM-CCD) camera (Model PhotonMAX: 1024B Air-Cooled, Princeton Instruments/Acton, USA) with a  $1024 \times 1024$  13- $\mu\text{m}$  pixel frame-transfer CCD detector, an imaging spectrograph (ImSpector V10E, Spectral Imaging Ltd., Oulu, Finland) covering the spectral region of 400–1000 nm, a focusing lens with a near-infrared enhanced lens, and a quartz tungsten halogen light source (Oriel Instruments, Stratford, Conn., USA) with an intensity controller. A computer installed with a frame grabber board and a program written in C++ was used for controlling the camera and acquiring images. For real-time acquisitions, an 8-foot long mini-line composed of a belt conveyor with sample holding cups and other control components was built. The speed of the belt was controlled by a servo motor, and apples were placed on the circular cups of 76 mm in diameter and 30 mm in height. The incident beam was 1.5 mm in size and the line scanning position of the camera was 1.6 mm off from the beam incident center to avoid saturation. The OHIS had an effective spectral region of 500–1090 nm with 1.65 nm nominal spectral resolution. The hyperspectral imaging system was enclosed in an imaging chamber to block ambient light.

The back-illuminated electron-multiplying CCD (EMCCD) camera with dual amplifiers was able to operate at 10 MHz for high-speed imaging or at 5 MHz for high precision photometry, and it was equipped with a deep thermoelectric cooling system oper-

ating at  $-55^\circ\text{C}$  to suppress system noise. Thus, the combination of EMCCD technology, large dynamic range (16-bit format), and on-chip multiplication gain was well suited for rapid online acquisition of scattering images from apples.

For each experimental run, fruit were manually loaded onto the sample cups on the conveyor with the stem–calyx end being aligned horizontally in perpendicular to the scanning line. Because of the manual loading speed limitation, the imaging system was run at a speed of approximately one fruit for every two seconds (or  $\sim 82$  mm/s for the conveyor speed), even though it was capable of capturing and processing images at a much higher speed. The OHIS captured and saved spectral scattering images for individual apples immediately after the two photoelectric beam sensors were triggered by the incoming cup and apple, respectively ([Fig. 1b](#)). The integration time was set at 120 ms for each apple. Preliminary testing showed that with this exposure time, the spectral scattering images remained sharp without distortion. The OHIS was set to acquire scattering images with the size of  $256 \times 256$  pixels using  $4 \times 4$  binning operations to allow faster image acquisition and processing.

### 2.3. Reference destructive measurements

After image recording of fruits, firmness and SSC were measured by standard destructive methods at the same location where the scattering measurements had been carried out. Magness–Taylor (MT) fruit firmness (N) measurements were performed with a texture analyzer (model TA.XT2i, Stable Micro Systems, Inc., Surrey, U.K.) with a steel probe of 11 mm diameter for a penetration depth of 9 mm at a loading speed of 2 mm/s. Maximum force recorded on the force/displacement curve was used as the measure of fruit firmness. Immediately after firmness measurements, juice was extracted and SSC (%) was measured using a digital refractometer (model PR-101, Atago Co., Tokyo, Japan). The equatorial diameter of each fruit was measured by a computerized image analysis tech-

nique developed in our lab, and this information was used later for correcting the fruit size effect on the scattering images.

#### 2.4. Pre-processing of scattering images for 1-D and 2-D data

The scattering images are symmetric with respect to the light incident point, and their intensity decreases rapidly as the distance from the light incident point increases (Fig. 2).

To obtain one-dimensional mean reflectance profile,  $pMeR$ , image preprocessing was carried out following the method proposed by Lu (2004). The brightest point in the dark-corrected scattering image ( $256 \times 256$  pixels) is first identified and taken as the center of the image. From this center the scattering image is split (in left and right sides) and the reflectance profile of each side is calculated by averaging over each wavelength. The resultant profiles (left and right) are averaged, size corrected (according to Peng and Lu, 2006), smoothed, and cropped to obtain a 1-D mean reflectance profile,  $R_{apple}$ , covering the spectral range of 500–1000 nm and a spatial range of 0–10 mm (see Fig. 2). Finally,  $R_{apple}$  is corrected by the mean reflectance  $R_{teflon}$  from a standard reference (a white Teflon disk, following the same imaging and preprocessing procedures as described for apple images) using the following equation:

$$pMeR = \frac{R_{apple}}{R_{teflon}}, \quad \text{for } 0 \leq x \leq 10 \text{ mm} \quad (1)$$

On the other hand, to obtain a two-dimensional reflectance image,  $iMeR$ , the brightest point in the dark-corrected scattering image ( $256 \times 256$  pixels) is first identified and taken as the center of the image. From this central axis, the scattering image is split (in left and right sides) and then averaged (pixel by pixel), size corrected (according to Peng and Lu, 2006), and cropped to obtain an  $iMeR$  of  $101 \times 72$  pixels, covering the spectral range of 500–1000 nm and a spatial range of 0–10 mm (Fig. 2). For image standardization ( $iMeR_{stand.}$ ), each pixel in the mean reflectance image is divided by the sum of the average of the 10 brightest pixels found in the dark-corrected standard reference image ( $Teflon_{avg10}$ ) and a factor of  $10^5$ . Addition of the factor in the denominator was to avoid image distortion due to the large intensity differences between the pixels around the light beam incident area and those in the scattering region (away from the beam). The obtained values were then multiplied by the same factor to enhance the intensity pixel values in the normalized image, which are calculated as follows:

$$iMeR_{stand.} = \frac{iMeR}{(Teflon_{avg10}) + 10^5} \times 10^5 \quad (2)$$

#### 2.5. Methods of analyzing 1-D scattering profiles

##### 2.5.1. Mean reflectance method ( $pMeR$ )

After computation of the mean scattering profile ( $pMeR$ ,  $101 \times 1$  points) as detailed above, the 101 wavelengths or data points were used in further partial least squares (PLS) analysis.

##### 2.5.2. Multi-resolution wavelet transform

Two simple methods based on multi-scale wavelet transform were tested: discrete wavelet transform ( $pDWT$ ) and continuous wavelet transform ( $pCWT$ ). For  $pDWT$  computation, a single-level one-dimensional decomposition using “symlet2” wavelet (Mallat, 1999) was carried out using the normalized mean scattering profile ( $pMeR$ ,  $101 \times 1$  points). Four discrete levels were computed from the spectrum, and two sets of coefficients were extracted for each level: approximation coefficients  $CA_1$ , and detail coefficients  $CD_1$ . These vectors were obtained by convolving the signal with the low-pass filter for approximation, and with the high pass filter for detail, followed by dyadic decimation. The resultant vector of coefficients for each scale was reduced by computing the root mean square for

each level. Thus, 8  $pDWT$  features ( $4 \text{ levels} \times 2 \text{ sets of coefficients}$ ) were derived from each scattering profile and used in further PLS analysis.

Continuous wavelet transform is a convolution product of a signal with a scaled and translated kernel (usually a  $n$ -th derivative of a smoothing kernel,  $\Psi$ , in order to precisely detect singularities).

$$Wf(u, s) = \frac{1}{s} \int_{-\infty}^{\infty} f(x) \psi \left( \frac{x-u}{s} \right) \cdot dx \quad (3)$$

where  $s$  and  $u$  are real numbers ( $s$  and  $u > 0$ ) which are discretized for computational purposes. In this way, the wavelet transform performs a transformation of a function  $f(x)$  into a function defined over the scale-space plane (pair of values  $u$  and  $s$ ). For  $pCWT$  computation, decomposition of the spectra was performed using a “symlet2” wavelet on the normalized mean scattering profile ( $101 \times 1$  points). Thirty-two scales were used for CWT decomposition, and the matrix of resultant coefficients for each scale was then reduced by computing the root mean square for each wavelength. Thus, 101  $pCWT$  features were derived from each scattering profile in the wavelength range of 500–1000 nm and used in further PLS analysis.

#### 2.6. Methods of analyzing 2-D scattering images

Two types of image processing methods were tested from the size-corrected and normalized scattering images ( $iMeR_{stand.}$ ) with the pixel size of  $101 \times 72$ : statistical texture analysis and multi-resolution wavelet transform for 2-D analysis.

##### 2.6.1. Grey level co-occurrence matrix (GLCM)

GLCM, which is probably the most frequently used method for statistical texture analysis, is based on the extraction of various textural features from a grey level co-occurrence matrix (GLCM) (Haralick et al., 1973). A GLCM is a matrix of size  $N_{grey} \times N_{grey}$  ( $N_{grey}$  is the number of grey levels) defined for a displacement of  $d$ -pixels along a given direction  $\theta$ . The entry  $P_{d\theta}(i, j)$  of this matrix is the number of occurrences of a pair of grey levels,  $i$  and  $j$ , for the specified displacement. Once the GLCM is defined, various textural descriptors can be evaluated as proposed by Haralick et al. (1973). However, four descriptors were chosen for analysis, namely, the energy, the entropy, the contrast as well as the correlation, which was the lowest possible correlation with each other. The scattering images were analyzed using four independent directions,  $\theta = 0, 45, 90, 135^\circ$ , as well as their average for a distance of  $d = 1$ . Thus, a total of 20 GLCM parameters were computed by the following equations:

$$\text{Energy} = \sum_i \sum_j P_{d\theta}(i, j)^2 \quad (4)$$

$$\text{Entropy} = - \sum_i \sum_j P_{d\theta}(i, j) \cdot \log(P_{d\theta}(i, j)) \quad (5)$$

$$\text{Contrast} = \sum_i \sum_j (i - j)^2 \cdot P_{d\theta}(i, j) \quad (6)$$

$$\text{Correlation} = \frac{\sum_i \sum_j (i \cdot j) p(i, j) - \mu_x \cdot \mu_y}{\sigma_x \cdot \sigma_y} \quad (7)$$

where  $\mu_i$  and  $\mu_j$  are the means, and  $\sigma_i$  and  $\sigma_j$  are the standard deviations. Energy measures the textural uniformity of the image, i.e., the repetition of pixel pairs. Entropy measures the disorder or randomness of the image and it is an indication of complexity within the image, i.e., more complex images have higher entropy values. Contrast is a measure of the local variations present in the image; so



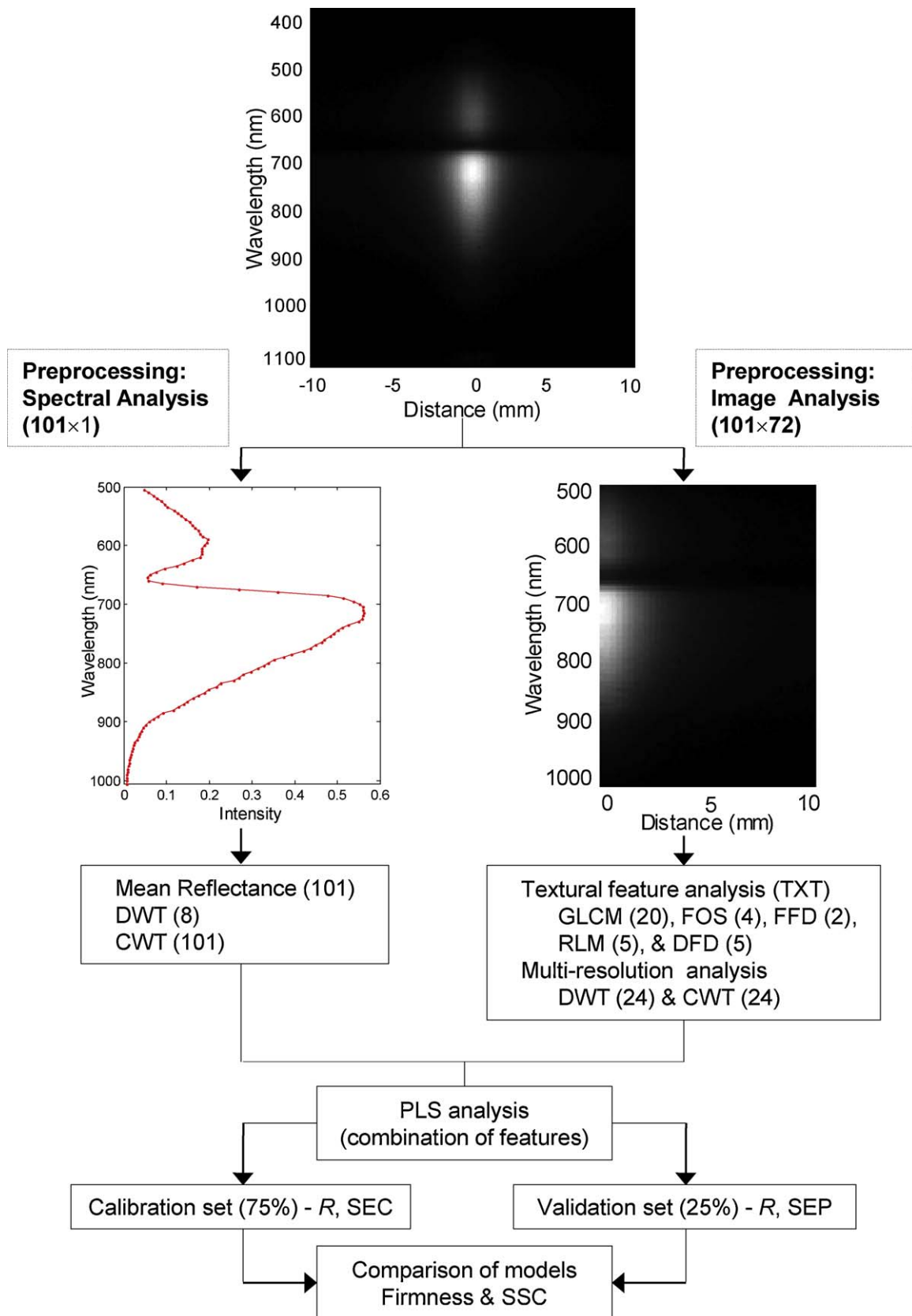


Fig. 2. Flowchart of image preprocessing and data analysis for predicting apple fruit quality.

higher contrast values indicate large local variations. Finally, correlation is a measure of image linearity among pixels (Mendoza et al., 2007).

#### 2.6.2. First-order statistics (FOS)

The features of FOS were derived from the normalized grey-level histogram of the scattering images of apples, which was built by counting the number of pixels ( $N$ ) with the grey value of  $i$  ( $I$ ) and can be written as:

$$H(i) = N \langle (x, y) | I(x, y) = i \rangle \quad (8)$$

The histogram,  $H(i)$ , is normalized using the function given below:

$$H'(i) = \frac{H(i)}{\sum_i H(i)} \quad (9)$$

The extracted statistical features for further PLS analysis included: mean of the pixel histogram ( $MV$ ), variance ( $VA$ ), entropy ( $ET$ ), and energy ( $EN$ ), which are defined as follows (Cernadas et al., 2005):

$$MV = \sum_i i H'(i) \quad (10)$$

$$VA = \sum_i (i - MV)^2 H'(i) \quad (11)$$

$$ET = - \sum_i H'(i) \log(H'(i)) \quad (12)$$

$$EN = \sum_i i^2 H'(i) \quad (13)$$

#### 2.6.3. Run length matrix (RLM)

First introduced by Galloway (1975), the grey-level RLM approach characterizes texture by the grey-level run, which is a set of consecutive pixels with the same grey-level. Run length is the number of pixels in a run. Therefore, the run length of coarse textures will be longer than that of fine textures. In RLM method, a matrix containing the information about the run length of images is constructed in terms of the brightness value and length of the runs (Fardet et al., 1998).

The run-length matrix  $P(i, j)$  is defined by specifying direction (i.e.,  $0^\circ, 45^\circ, 90^\circ, 135^\circ$ ) and then counting the occurrence of runs for each grey levels and length in this direction.  $i$  – dimension corresponds to the grey level (bin values) and has a length equal to the maximum grey level (bin values),  $j$  – dimension corresponds to the run length and has length equal to the maximum run length (bin values). Five features proposed by Galloway (1975), i.e., short run emphasis ( $SRE$ ) which measures the distribution of short runs, long run emphasis ( $LRE$ ) which measures the distribution of long runs, grey-level non-uniformity ( $GLNU$ ) which measures the similarity of grey level values throughout the image, run length non-uniformity ( $RLNU$ ) which measures the similarity of the length of runs throughout the image, and run length percentage ( $RLP$ ) which measures the homogeneity and the distribution of runs of an image in a given direction, were computed for further PLS analysis and are described as follows:

$$SRE = \frac{1}{n_r} \sum_{i=1}^M \sum_{j=1}^N \frac{P(i, j)}{j^2} \quad (14)$$

$$LRE = \frac{1}{n_r} \sum_{i=1}^M \sum_{j=1}^N P(i, j) \cdot j^2 \quad (15)$$

$$GLNU = \frac{1}{n_r} \sum_{j=1}^N \left( \sum_{i=1}^M P(i, j) \right)^2 \quad (16)$$

$$RLNU = \frac{1}{n_r} \sum_{i=1}^M \left( \sum_{j=1}^N P(i, j) \right)^2 \quad (17)$$

$$RLP = \frac{n_r}{n_p} \quad (18)$$

In the above,  $n_r$  is the total number of runs and  $n_p$  is the number of pixels in the image,  $M$  is the number of grey levels (bins) and  $N$  is the number of run length (bins). The scattering images were evaluated using the average of the four directions, i.e.,  $0, 45, 90, 135^\circ$  for each RLM matrix feature.

#### 2.6.4. Fourier fractal texture (FFT)

The methods to calculate fractal dimensions can be divided into two types: spatial and spectral. The first type operates in the spatial domain, while the second type operates in the frequency domain, using the Fourier power spectrum. The two types are unified by the principle of fractional Brownian motion (Dougherty and Henebry, 2001). The power spectrum method is based on its dependence of fractional Brownian motion. The 2-D Fourier transform of the apple scattering image was calculated first and then the 2-D power spectrum was derived. The 2-D power spectrum was reduced to a 1-D radial power spectrum (direction-independent mean spectrum, i.e., the average of all possible directional power spectra) by averaging values over increasingly larger annuli for each of the radial increments (Dougherty and Henebry, 2001). The power spectrum,  $P(f)$ , varying with frequency  $f$ , is calculated as follows:

$$P(f) = k \cdot f^{(-1-2H)} \quad (19)$$

where  $k$  is a constant and  $H$  is the Hausdorff–Besicovitch dimension. When the  $\log[P(f)]$  is plotted against  $\log[f]$ , a straight line can be fitted. According to the Fourier slice theorem, the 1-D Fourier transform of a parallel projection of an image along a line with the direction  $h$  is identical to the value along the same line in the 2-D Fourier transform of the image. This means that the line through the spectrum gives the spectral information obtained from a projection with the same orientation in the spatial domain. FFT dimensions,  $D_f$ , were calculated as a function of orientation based on this theorem, with 24 being the number of directions that the frequency space was uniformly divided. The data of magnitude vs. frequency are plotted in log–log scale and its slope is determined using linear least-squares regression. Thus, the Hausdorff–Besicovitch dimension  $H$  is computed from the slope  $c$  of the straight line,  $c = (-1 - 2H)$ . The  $D_f$  dimension of the apple scattering image is related to the slope  $c$  of the log–log plot by the equation below, with  $H = D_f - 3$ ,  $2 < D_f < 3$  and  $3 < c < 1$  (Geraets and Van der Stelt, 2000):

$$D_f = \frac{7}{2} + \frac{c}{2} \quad (20)$$

The slope and intercept for all directions were computed from each scattering image and used for further PLS analysis. The algorithm used was originated from Russ (2005), and was modified in the current study. Details of the method can be found in Valous et al. (2009).

#### 2.6.5. Variogram method for directional fractal dimension analysis (DFD)

A fractal describes a rough or fragmented geometric shape that can be subdivided into parts, each of which is, at least approximately, a reduced-size copy of the whole. This means that they are generally self-similar and independent of scale. The estimated

fractal dimension of these images represents the roughness of the clutter at various scales. The computation of the DFD of scattering images using variogram model is (Kube and Pentland, 1988; Mandelbrot, 1982):

$$\nu(d) = c \cdot d^a$$

$$\nu(d) = \frac{1}{N(d)} \sum_{N(d)} [y(s+d) - y(s)]^2 \quad (21)$$

$$DFD = 3 - 0.5\hat{a}$$

where  $\nu(d)$  is the variogram of the image,  $a$  is termed the fractal index,  $c$  is a constant,  $d$  is the separation distance in pixels,  $y(s)$  denotes the grey level of the pixel at location  $s$ , and  $N(d)$  denotes the cardinality of the set of pairs of observations. The image variogram  $\nu(d)$  represents the variance or dispersion of the difference between two random variables. Thus, the relationship between  $a$  and  $\nu(d)$  can also be represented using a linear regression model by applying log function to both sides of this equation and to get an estimate of fractal index  $\hat{a}$ . Then, the directional fractal dimension (DFD) of the image can be directly computed.

The variogram of the image and hence the fractal dimension is estimated at a fixed image resolution level without specifying any spatial direction along which the set of pairs of observations is constructed (Mendoza et al., 2009). This means that the image is assumed to be isotropic. Since the fractal texture parameters of apples could not be expected to have isotropic patterns, four variograms, which are computed along the directions  $d = 0^\circ$ ,  $45^\circ$ ,  $90^\circ$ , and  $135^\circ$  respectively (namely horizontal, first diagonal, vertical and second diagonal), were analyzed and averaged for a given pixel location  $s$  of a given image. A total of 5 DFD features were computed ( $DFD_{0^\circ}$ ,  $DFD_{45^\circ}$ ,  $DFD_{90^\circ}$ ,  $DFD_{135^\circ}$ , and  $DFD_{avg}$ ) and used in further PLS analysis.

#### 2.6.6. Multi-resolution wavelet transform

Image scale is important for texture analysis because there might be several different textures in the same image with different scales. However, traditional approaches for image texture analysis, such as RLM and GLCM methods, are limited in that they are restricted to the analysis of an image over a single scale. Recent developments in multi-scale analysis methods, such as wavelet transform, have proven that these methods are useful to characterize different scales of texture effectively. Wavelet transform has both a solid theoretical foundation and good empirical performance in multi-scale image analysis. In this research two methods were tested on the scattering images: discrete wavelets transform (*iDWT*) and continuous wavelets transform (*iCWT*).

For implementation of the methods, first a number of wavelet transforms were tested (i.e., Daubechies (4), symlet (2–4), haar and coiflet (3)) to evaluate the prediction performance on firmness and SSC. The best prediction values were obtained using “symlet2” wavelet transform for the three apple cultivars. For *iDWT* computation, 2-D decomposition using “symlet2” wavelet was carried out using the normalized mean scattering image ( $101 \times 72$  pixel). Six discrete levels were computed from the image, and four sets of coefficients were extracted from each level. Each decomposition level at a particular order yields a horizontal, vertical, diagonal and approximation coefficient. The resultant vector of coefficients for each scale was obtained by computing the root mean square for each level. Thus, 24 *iDWT* features (6 levels  $\times$  4 sets of coefficients) were derived from each scattering image and used in further PLS analysis.

For *iCWT* computation, the extension of the previous concept from 1-D [Eq. (2)] to 2-D is given by Piñuela et al. (2007):

$$Mf(u, v, s) = \sqrt{|W^1 f(u, v, s)|^2 + |W^2 f(u, v, s)|^2} \quad (22)$$

with  $u$  and  $v$  denoting the 2-D coordinates and the scale parameter being usually used as  $s = 2^j$ . Now, two separate wavelet transforms are computed:  $W^1$  refers to the wavelet transform performed along the horizontal dimension (i.e., space) and  $W^2$  refers to the vertical one (i.e., wavelength). In this study, *iCWT* was computed for 24 consecutive scales along the vertical and horizontal dimensions. The resultant matrix of coefficients for each scale  $s$  was obtained by computing the root mean square for each level. Thus, 24 *iCWT* features were derived from each scattering image and used in further PLS analysis.

#### 2.7. Scattering features integration

For predicting firmness and SSC, a single spectrum is needed for each sample. Parameters generated from the scattering profile methods and image analysis methods are different greatly in their scale of values. Single spectra could be created by simply combination of two independent or multiple parameters into one, i.e., connecting them together in a vector. In this study, the vector of combined features from each apple was built by placing the extracted data consecutively one after another. A potential problem with this preprocessing method is that a large-value parameter would have a dominant predicting power over smaller value parameter(s), even though the latter may be as important as, or even more important than, the former. In this study, an autoscaling method was used to overcome the problem of large disparity in values among the function parameters. Autoscaling is essentially a normalization procedure, which is given as follows:

$$Y_{N,i} = \frac{Y_i - \bar{Y}}{SD} \quad (23)$$

where  $Y_{N,i}$  denotes the rescaled parameter for sample  $i$  at a given scattering profile or image feature,  $\bar{Y}$  is the mean value of the calibration samples,  $SD$  is the corresponding standard deviation, and  $Y_i$  is the original parameter for sample  $i$ . This preprocessing procedure rescales spectra of parameters to zero means and unit variance. After rescaling, each parameter would preserve its essential features but have a similar scale of values. A new single spectrum was created by progressive clustering of selected profile features or/and image features one after another. This procedure was applied to both calibration and validation samples to create new spectra for each scattering characterization method. After the spectra had been created, partial least squares (PLS) method was then applied to develop calibration models for firmness and SSC for each testing set of combined features.

#### 2.8. Calibration models for firmness and SSC prediction

PLS regression is a widely used chemometric method for building calibration models. PLS is suited well when the matrix of predictors has more variables than observations, and also when the input variables contain noise and are strongly correlated. PLS components are computed under the constraint of maximization of covariance between inputs and outputs. Therefore, it can provide a set of orthogonal factors that have the best predictive power from the combinations of different methods with an increased number of variables.

Prior to the model development, samples for each cultivar were first sorted in ascending order for firmness or SSC. The sorted samples were then divided into two groups: 75% of the samples were used for calibration and the remaining 25% samples were used for independent validation (or prediction). In this study, PLS models (i.e., selection of appropriate numbers of latent variables) were determined by full cross-validation of the calibration set until the root-mean-square error of cross validation (RMSECV) reached minimum. After a calibration model was developed, it was then used to

**Table 1**  
Statistics of reference quality measurements for test apple samples.

Apple variety	Quality parameter	Maximum	Minimum	Mean	SD
Golden Delicious (year 2006, 600 apples)	Firmness (N)	88.5	31.2	56.6	12.1
	SSC (%)	15.7	8.0	10.7	1.4
	Diameter (mm)	82.8	59.6	69.8	3.3
Jonagold (year 2009, 928 apples)	Firmness (N)	125.0	29.3	64.3	22.8
	SSC (%)	16.8	9.3	12.7	1.1
	Diameter (mm)	101.6	65.8	78.8	6.6
Delicious (year 2009, 1191 apples)	Firmness (N)	100.2	25.6	56.7	15.8
	SSC (%)	16.4	8.1	11.5	1.2
	Diameter (mm)	81.2	60.9	67.4	3.3

predict the independent set of samples that had not been used in calibration. More detailed explanation of the PLS regression analysis coupled with leave-one-out cross validation is given in [Qin et al. \(2009\)](#).

To obtain the optimal combinations of spectral and image texture analysis methods for improving firmness and SSC prediction, preliminary comparisons of individual methods were performed, which resulted in the selection of 32 combinations of methods. These combinations were obtained, first, by integrating the methods with the highest correlation coefficients and lowest standard errors for prediction (SEP) when used alone, and then progressively adding new combinations to the best previous combinations (i.e., increasing the number of methods or features for PLS analysis) until all methods or features had been tested and evaluated. By this point, the PLS modeling process would be considered complete according to the standard procedure of chemometric modeling. However, this research went one step further by repeating the above calibration/cross validation and prediction procedures on new sets of calibration and prediction samples. These new sets of calibration and prediction samples were created by returning the prediction samples (i.e., the 1/4 of all samples) to the calibration set in the first round of model development and then taking out another 1/4 samples from the calibration set as an independent set of prediction samples. The same procedures described above were again applied for model calibration, cross validation and prediction. The process was repeated four times (i.e., each time 1/4 samples were taken out as prediction samples). Finally, *t*-test was performed on the average SEPs for the four runs or iterations of individual methods and their combinations to determine their statistical differences. Due to the large number of features (294 in total), the optimal sets of features selected for each run might not be exactly the same for the same cultivars of apple.

[Fig. 2](#) is a flowchart showing the main steps for feature extraction from the hyperspectral scattering images of GD, JG and RD apples. Algorithms for pre-processing full images, profile scattering analysis, and image scattering analysis were written in MATLAB 7.5.0 (The MathWorks, Inc., MA, USA). PLS regression analysis was performed using the PLS Toolbox v5.0 in conjunction with MATLAB (Eigenvector Research, Inc, WA, USA).

### 3. Results and discussion

#### 3.1. Quality characterization of test apples

The statistics of fruit firmness, SSC, and size for the three apple cultivars are summarized in [Table 1](#). A relatively large range of firmness distributions for the three cultivars was observed, which was especially evident for JG apples. It is, however, important to note that the firmness distributions of JG and RD were not uniform around the range of 55–70 N; there were fewer samples in this region (not less than 50 apples using a 5 N histogram bin size of firmness). Contrarily, SSC showed a Gaussian-shaped distribu-

tion with the standard deviation (SD) ranging from 1.1% for JG to 1.4% for GD.

It is worth mentioning the size and shape of apples for each cultivar. Overall, GD apples were conical and JG apples were round; the fruit for both cultivars were relatively uniform in shape. In contrast, RD apples were of conical and elongated shape, with an uneven surface, which could negatively affect the measurement of light scattering ([Peng and Lu, 2006](#)). Measurements of apple diameters showed that JG apples had the largest range of sizes, whose standard deviation was twice that for GD and RD apples. The curved fruit surface would cause the underestimation of scattering intensities for locations away from the incident center. Hence the fruit size–curvature effect on the scattering intensity measurements was corrected according to [Peng and Lu \(2006\)](#).

#### 3.2. PLS prediction of firmness and SSC

In this research, the performance and improvement of the prediction models for assessing firmness and SSC was evaluated and compared against that of the *pMeR* (i.e., mean reflectance) method ([Peng and Lu, 2006](#)). It is important to note that in this study, the extracted features for the 1-D and 2-D data involved averaging the left and right split scattering images. For the 1-D data analysis, spectral profiles for the left and right sides for each wavelength were averaged to obtain the mean scattering profiles. For the 2-D image data, the split images for the left and right sides were averaged pixel by pixel to obtain a mean scattering image. While this procedure generally reduced noise, it has also evened out the differences between the two-side images or 1-D scattering profiles, which might have removed some useful information. However, preliminary analysis for the three apple cultivars showed that differences between the left and right scattering profiles were small with the coefficient of variability being smaller than 5% for the 10 mm scattering distance. Additionally, preliminary comparisons of the prediction results between whole images (202 × 144 pixels) and mean images (101 × 72 pixels), based on image texture and multi-resolution analysis features, did not show significant differences ( $p < 0.05$ ).

[Table 2](#) summarizes firmness predictions for GD, JG and RD apples using PLS method with different combinations of spectral and image features (i.e., *pMeR* + *pDWT* + *pCWT* + *TXT* + *iDWT* + *iCWT*). Similarly, [Table 3](#) presents SSC predictions using PLS method with the best combination of features (i.e., *pMeR* + *pDWT* + *pCWT* + *iDWT*) for GD, JG and RD apples, respectively. Listed in [Tables 2 and 3](#) are only those combinations of features that improved the average SEP (i.e., average of four iterations) for two or more cultivars by at least 5% for firmness and 2% for SSC, when compared with the *pMeR* method. Moreover, to avoid overloading, [Tables 2 and 3](#) do not provide complementary information of the analysis, such as standard deviations. However, it should be emphasized that there were low variations between the four iterations in terms of *R*s and SEPs. With all combined methods for firmness prediction, the average standard deviations for  $R_{pred}$  varied between 0.02 and 0.03 for



**Table 2**  
Average prediction results of firmness for Golden Delicious, Jonagold, and Delicious apples.

Firmness Feature – combinations	Golden Delicious						Jonagold						Delicious					
	Avg. fact.	$\bar{R}_{cal}$	$\overline{SEC}$	$\bar{R}_{pred}$	$\overline{SEP}$	Dif. (%)	Fact.	$\bar{R}_{cal}$	$\overline{SEC}$	$\bar{R}_{pred}$	$\overline{SEP}$	Dif. (%)	Fact.	$\bar{R}_{cal}$	$\overline{SEC}$	$\bar{R}_{pred}$	$\overline{SEP}$	Dif. (%)
<i>pMeR</i> (101)	10	0.871	5.92	0.852	6.30 <sup>A</sup>		23	0.945	7.44	0.929	8.50 <sup>A</sup>		21	0.819	9.03	0.769	10.12 <sup>A</sup>	
<i>pMeR</i> + <i>pDWT</i> + <i>pCWT</i> (210)	13	0.882	5.69	0.873	5.91 <sup>B</sup>	6.3	24	0.952	6.96	0.934	8.16 <sup>A</sup>	3.9	26	0.856	8.14	0.803	9.46 <sup>B</sup>	6.5
<i>pCWT</i> + <i>iDWT</i> (125)	16	0.882	5.69	0.869	5.98 <sup>A</sup>	5.1	38	0.956	6.71	0.943	7.57 <sup>B</sup>	10.9	25	0.832	8.74	0.797	9.56 <sup>A</sup>	5.5
<i>pMeR</i> + <i>iDWT</i> + <i>iCWT</i> (149)	16	0.876	5.81	0.858	6.21 <sup>A</sup>	1.4	19	0.96	6.42	0.948	7.29 <sup>B</sup>	14.2	29	0.853	8.21	0.797	9.59 <sup>A</sup>	5.2
<i>pDWT</i> + <i>pCWT</i> + <i>iDWT</i> + <i>iCWT</i> (157)	17	0.888	5.54	0.873	5.89 <sup>B</sup>	6.6	33	0.959	6.44	0.948	7.30 <sup>B</sup>	14.0	33	0.847	8.37	0.801	9.52 <sup>A</sup>	6.0
<i>pMeR</i> + <i>iTXT</i> + <i>iDWT</i> (161)	24	0.885	5.62	0.858	6.23 <sup>A</sup>	1.2	26	0.963	6.14	0.947	7.32 <sup>B</sup>	13.9	34	0.875	7.61	0.818	9.13 <sup>B</sup>	9.8
<i>pMeR</i> + <i>pCWT</i> + <i>iDWT</i> (226)	15	0.884	5.63	0.869	5.99 <sup>A</sup>	5.0	30	0.966	5.93	0.949	7.25 <sup>B</sup>	14.7	29	0.864	7.93	0.807	9.39 <sup>B</sup>	7.3
<i>pMeR</i> + <i>pCWT</i> + <i>iCWT</i> (226)	14	0.883	5.65	0.869	5.99 <sup>A</sup>	5.0	31	0.956	6.70	0.934	8.22 <sup>A</sup>	3.3	25	0.858	8.10	0.804	9.44 <sup>B</sup>	6.7
<i>pMeR</i> + <i>pDWT</i> + <i>pCWT</i> + <i>iDWT</i> (234)	16	0.889	5.53	0.874	5.89 <sup>B</sup>	6.6	24	0.963	6.11	0.949	7.22 <sup>B</sup>	15.0	31	0.866	7.86	0.804	9.49 <sup>B</sup>	6.3
<i>pMeR</i> + <i>pCWT</i> + <i>iDWT</i> + <i>iCWT</i> (250)	16	0.884	5.63	0.868	6.00 <sup>A</sup>	4.7	30	0.966	5.91	0.948	7.28 <sup>B</sup>	14.3	29	0.868	7.83	0.810	9.33 <sup>B</sup>	7.8
<i>pMeR</i> + <i>pDWT</i> + <i>pCWT</i> + <i>iTXT</i> + <i>iDWT</i> + <i>iCWT</i> (294)	20	0.893	5.43	0.863	6.12 <sup>A</sup>	2.9	26	0.966	5.90	0.950	7.13 <sup>B</sup>	16.1	33	0.893	7.09	0.835	8.73 <sup>B</sup>	13.7

Avg. Fact.: average number of features required for the model after optimization;  $\bar{R}_{cal}$  and  $\bar{R}_{pred}$ : average correlation coefficients of calibration and prediction, respectively, over four calculations.  $\overline{SEC}$  and  $\overline{SEP}$ : average standard error for calibration and prediction, respectively, over four calculations. Dif.(%): percent difference in the  $\overline{SEP}$  between the mean reflectance method (*pMeR*) and the selected combination of features. <sup>A,B</sup>  $\overline{SEP}$  columns with different letters represent statistical differences (*t*-test = 0.05) between the mean reflectance method (*pMeR*) and tested combinations.

**Table 3**  
Average prediction results of soluble solids content (SSC) for Golden Delicious, Jonagold, and Delicious apples.

SSC Feature - combinations	Golden Delicious						Jonagold						Delicious					
	Avg. Fact.	$\bar{R}_{cal}$	$\overline{SEC}$	$\bar{R}_{pred}$	$\overline{SEP}$	Dif.(%)	Fact.	$\bar{R}_{cal}$	$\overline{SEC}$	$\bar{R}_{pred}$	$\overline{SEP}$	Dif.(%)	Fact.	$\bar{R}_{cal}$	$\overline{SEC}$	$\bar{R}_{pred}$	$\overline{SEP}$	Dif.(%)
<i>pMeR</i> (101)	10	0.875	0.67	0.842	0.75 <sup>A</sup>		10	0.793	0.69	0.762	0.74 <sup>A</sup>		18	0.706	0.86	0.623	0.96 <sup>A</sup>	
<i>pMeR</i> + <i>pDWT</i> + <i>pCWT</i> (210)	23	0.911	0.57	0.863	0.70 <sup>A</sup>	6.1	21	0.818	0.65	0.765	0.74 <sup>A</sup>	−0.1	26	0.733	0.83	0.646	0.94 <sup>A</sup>	2.1
<i>pMeR</i> + <i>iDWT</i> (125)	24	0.911	0.57	0.867	0.69 <sup>A</sup>	7.5	33	0.845	0.61	0.774	0.73 <sup>A</sup>	1.8	29	0.741	0.82	0.647	0.94 <sup>A</sup>	2.4
<i>pMeR</i> + <i>pDWT</i> + <i>iDWT</i> (133)	29	0.919	0.54	0.865	0.70 <sup>A</sup>	6.5	34	0.847	0.60	0.767	0.74 <sup>A</sup>	0.1	28	0.74	0.82	0.648	0.94 <sup>A</sup>	2.5
<i>pMeR</i> + <i>iDWT</i> + <i>iCWT</i> (149)	25	0.914	0.56	0.866	0.70 <sup>A</sup>	6.9	28	0.840	0.62	0.766	0.74 <sup>A</sup>	0.3	30	0.743	0.81	0.650	0.93 <sup>A</sup>	2.8
<i>pMeR</i> + <i>pCWT</i> + <i>iDWT</i> (226)	25	0.907	0.58	0.876	0.67 <sup>B</sup>	10.8	28	0.837	0.62	0.771	0.73 <sup>A</sup>	0.9	30	0.751	0.80	0.649	0.94 <sup>A</sup>	2.3
<i>pMeR</i> + <i>pCWT</i> + <i>iCWT</i> (226)	18	0.898	0.61	0.870	0.68 <sup>B</sup>	8.9	30	0.845	0.60	0.777	0.73 <sup>A</sup>	1.9	26	0.742	0.82	0.648	0.94 <sup>A</sup>	2.3
<i>MeR</i> + <i>pDWT</i> + <i>pCWT</i> + <i>iDWT</i> (234)	26	0.911	0.57	0.877	0.67 <sup>B</sup>	11.2	16	0.814	0.66	0.774	0.72 <sup>A</sup>	2.3	30	0.752	0.80	0.656	0.91 <sup>B</sup>	3.0
<i>pMeR</i> + <i>pDWT</i> + <i>pCWT</i> + <i>iTXT</i> + <i>iDWT</i> (270)	32	0.911	0.57	0.869	0.68 <sup>B</sup>	8.7	17	0.821	0.65	0.777	0.71 <sup>B</sup>	2.8	36	0.766	0.78	0.654	0.93 <sup>A</sup>	2.6
<i>pMeR</i> + <i>pCWT</i> + <i>iDWT</i> + <i>iCWT</i> (250)	29	0.916	0.55	0.871	0.69 <sup>A</sup>	8.5	17	0.817	0.65	0.774	0.72 <sup>A</sup>	2.3	29	0.750	0.80	0.652	0.93 <sup>A</sup>	2.7
<i>pMeR</i> + <i>pDWT</i> + <i>pCWT</i> + <i>iTXT</i> + <i>iDWT</i> + <i>iCWT</i> (294)	32	0.911	0.57	0.868	0.69 <sup>A</sup>	8.4	17	0.822	0.65	0.778	0.71 <sup>B</sup>	3.0	36	0.767	0.78	0.677	0.90 <sup>B</sup>	3.0

Avg. Fact.: average number of features required for the model after optimization.  $\bar{R}_{cal}$  and  $\bar{R}_{pred}$ : average correlation coefficients of calibration and prediction, respectively, over four calculations.  $\overline{SEC}$  and  $\overline{SEP}$ : average standard error for calibration and prediction, respectively, over four calculations. Dif.(%): percent difference in the  $\overline{SEP}$  between the mean reflectance method (*pMeR*) and the selected combination of features. <sup>A,B</sup>  $\overline{SEP}$  columns with different letters represent statistical differences (*t*-test = 0.05) between the mean reflectance method (*pMeR*) and tested combinations.

GD, 0.0 and 0.01 for JG, and 0.0 and 0.02 for RD; and the average standard deviations for SEP varied between 0.41 and 0.55 for GD, 0.14 and 0.43 for JG, and 0.12 and 0.44 for RD. Similarly, for SSC prediction, the average standard deviations for  $R_{\text{pred}}$  varied between 0.01 and 0.03 for GD and RD, and 0.01 and 0.02 for JG; and the average standard deviations for SEP varied between 0.03 and 0.07 for GD, 0.01 and 0.03 for JG, and 0.0 and 0.03 for RD.

The *pCWT* method had the best predictions for both firmness and SSC for all cultivars with the average firmness correlation coefficient of prediction,  $R_{\text{pred}}$ , being 0.865, 0.925 and 0.793 and the average SEP of 6.1, 8.8 and 9.6 N for GD, JG, and RD, respectively. For SSC, the average  $R_{\text{pred}}$  values were 0.852, 0.740 and 0.598, and the average SEP values were 0.73, 0.77 and 0.98% for GD, JG, and RD, respectively. With the *pCWT* method, the average SEP for firmness for GD and RD was reduced by 3.8% and 4.7%, respectively, compared with those obtained with the *pMeR* method. However, SSC improvements were achieved only for GD; *pCWT* reduced the average SEP by 2.9% compared with the *pMeR* method.

Overall, integration of image analysis features based on the texture and multi-resolution wavelet transform methods was more effective for improving firmness predictions than for SSC predictions. For the three apple cultivars tested using the two different hyperspectral imaging setups, features combinations involving wavelet transform-based methods (i.e., DWT and CWT) for either 1-D scattering profile or 2-D image analysis had the strongest correlation with firmness, while their correlation with SSC was less significant. With the best combinations of features, the average SEP for firmness for GD, JG, RD apples was significantly reduced (by the *t*-test) by 6.6, 16.1, 13.7%, respectively ( $R_{\text{pred}}$  of 0.87, 0.95, 0.84 and the SEP of 5.9, 7.1, 8.7 N), and by 11.2, 2.3 (not significant), and 3.0% for SSC ( $R_{\text{pred}}$  of 0.88, 0.77, 0.66 and SEP of 0.7, 0.7, 0.9%), respectively.

Higher correlations for the wavelet transform-based methods over the texture analysis methods (GLCM, FOS, FFT, RLM and DFD) could be because the former provided better analysis of spatial interactions over relatively small neighborhoods on a single scale. Scale is related to the size of the textural elements on the image, and therefore, strong relationships between wavelet transform characteristics and apple firmness could be expected. It is important to note that combinations of profiles and image features resulted in greater improvements for firmness predictions with the use of the OHIS than those using SHIS. In contrast, combinations of features had greater contributions to improving SSC predictions with the SHIS than those using OHIS. An important difference between SHIS and OHIS was the size of the light beam impinging the apple surface. The larger light beam in OHIS produced larger scattering images on the surface, which could help to provide more details about image contrast, entropy and specific pixel arrangement or pixel pattern on the image. This allowed better characterization of the scattering intensity distribution by the textural and multi-resolution methods and, thus, better prediction of the MT-firmness of the fruit. However, this preliminary observation needs to be confirmed since the hyperspectral systems were not compared using the same sets of apples. The light beam in the SHIS was arranged perpendicular to the scan line, while the light beam in the OHIS was set parallel to the scan line. This difference could also influence the performance of the two systems.

Fig. 3 shows firmness and SSC predictions obtained with the best combinations of features (*pMeR*+*pDWT*+*pCWT*+*iDWT* for GD apples and *pMeR*+*pDWT*+*pCWT*+*iTXT*+*iDWT*+*iCWT* for JG and RD apples) (see Tables 2 and 3 respectively). Much better firmness predictions ( $R_{\text{pred}}$ =0.950 and SEP=7.13 N) were obtained for JG, compared with those for GD and RD. Since the firmness distributions for the three cultivars were quite different (Table 1), further comparison of firmness predictions for the three cultivars was performed in terms of the residual predictive deviation (RPD), i.e.,

the ratio of sample standard deviation to the standard error of prediction. The RPD values for JG, GD and RD were 3.2, 2.0, and 1.8 respectively. Better firmness predictions for JG may have been attributed to several factors. First, JG apples had a greater range of firmness distribution, which is generally favorable for the model development. Second, JG apples used in the experiment were of better quality based on visual inspection and were free from visible surface defect. In comparison, many GD and RD apples had various degrees of surface defect (i.e., scab and russet), which could have had a negative effect on the acquisition of scattering images. In addition, JG apples were of regular shape compared to RD apples. Firmness prediction results for GD and RD obtained with the best combinations of spectral and image features in this research are comparable to those reported in previous studies (Lu, 2007).

Good SSC predictions were obtained for GD apples ( $R_{\text{pred}}$ =0.877 and SEP=0.67%), whereas relatively poor results were obtained for JG and RD apples ( $R_{\text{pred}}$ =0.778 and 0.678 and SEP=0.72 and 0.90% respectively) (Fig. 3). The RPD values for GD, JG, and RD were 2.1, 1.6 and 1.3 respectively. These results are not as good as the firmness prediction results, and they also compare poorly with NIR reflectance technique (Lammertyn et al., 1998; Lu et al., 2000). The trend of having better firmness prediction over SSC prediction for spectral scattering technique was also observed in our previous studies (Lu, 2004, 2007; Lu et al., 2009). This suggests that spectral scattering technique may be inherently inferior for SSC measurement because its sensing configuration tends to enhance scattering features, thus resulting in better firmness prediction but not in SSC.

The hyperspectral image data for the 600 GD apples obtained by SHIS were also used by Qin et al. (2009), from which they determined the absorption and scattering coefficient spectra ( $\mu_a$  and  $\mu'_s$ , respectively) for the wavelengths of 500–1000 nm using a diffusion theory model coupled with an inverse algorithm. Qin et al. demonstrated that the combined data of  $\mu_a$  and  $\mu'_s$  gave better predictions of fruit firmness and SSC ( $R_{\text{pred}}$ =0.857 and 0.754 with the corresponding SEP of 6.07 N and 0.90%, respectively) than if each parameter was used alone. They further showed that the *pMeR* method gave comparable firmness predictions and better SSC predictions. Later, Lu et al. (2009) confirmed that using the same set of GD apples, the mean reflectance method yielded results similar to those obtained using a modified four-parameter Lorentzian function ( $R_{\text{pred}}$ =0.860, SEP=6.2 for firmness and  $R_{\text{pred}}$ =0.828, SEP=0.80 for SSC). This research has shown that for the same set of GD apples and two other sets of JG and RD apples, prediction models integrating spectral scattering and image characteristics significantly improved firmness and SSC prediction results compared with the mean reflectance method when used alone.

In this research, the algorithms developed for the 10 different spectral and image analysis techniques were not optimized for real-time prediction of fruit firmness and SSC. Nevertheless, these algorithms were still able to achieve fast pre-processing and extraction of features from each apple image (approximately 1 s using an Intel Xeon Dual Core PC with 2.4 GHz CPU, 6.0-GB RAM, and 256-GB hard disk). After the calibration model was built, prediction results using the PLS-Toolbox were obtained instantaneously. Hence, it is feasible to implement these techniques in real time situations.

This research has shown that integration of spectral and image features for hyperspectral scattering technique significantly improved firmness and SSC prediction (by the *t*-test) for all three cultivars but with a lesser degree of pronouncement for SSC. With the improved methods for scattering image analysis, the technique is moving closer toward the goal of real-time measurement and grading of fruit for firmness and SSC. The authors will continue to improve and refine the system to meet the on-line sorting requirements for apples. In addition, fusion with other nondestructive sensing techniques, such as near-infrared reflectance, fluorescence,

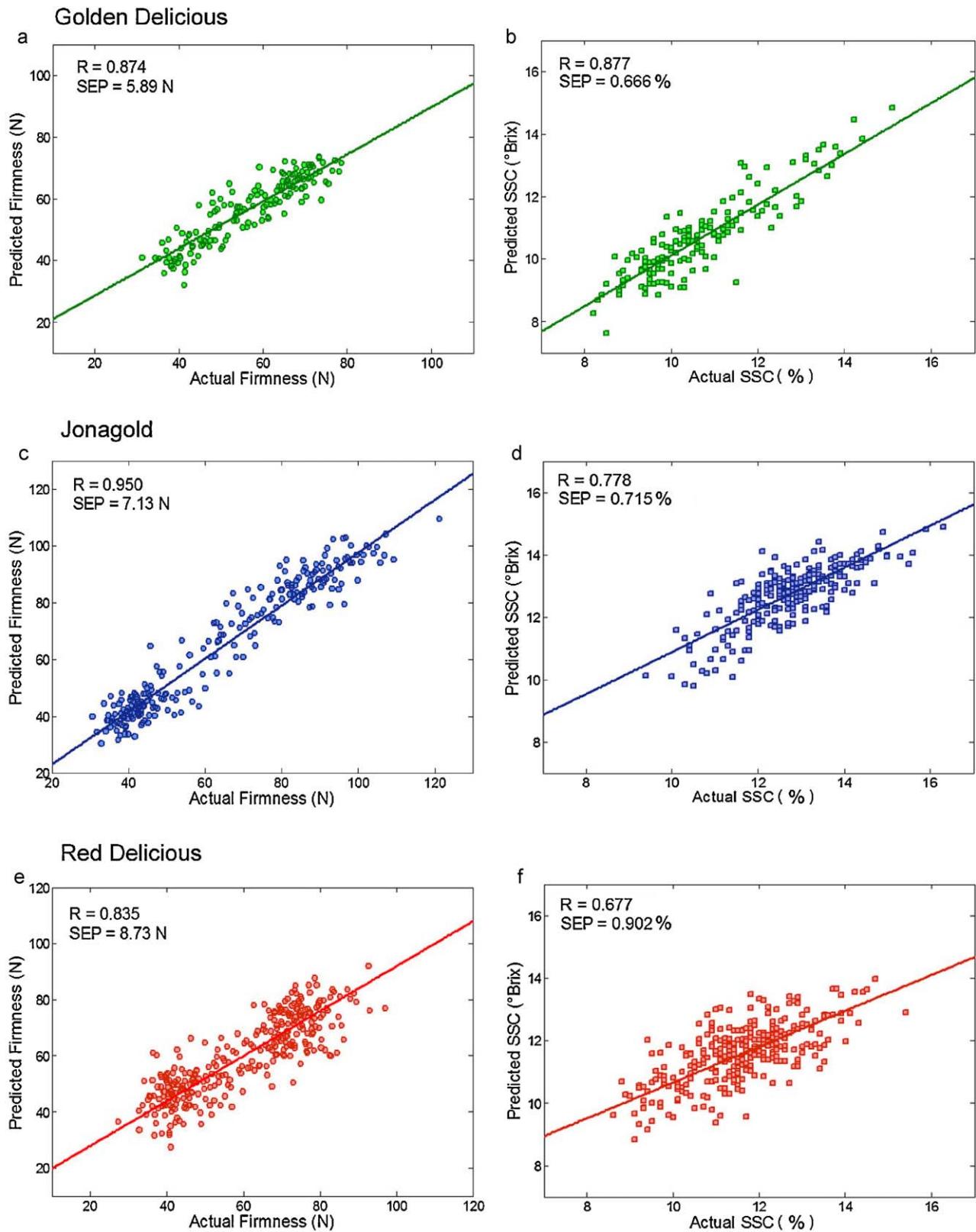


**Fig. 3.** Firmness (a, c, e) and soluble solids content (SSC) (b, d, f) predictions using the best combinations of spectral and image features for Golden Delicious, Jonagold and Red Delicious apples.

and/or acoustic, could lead to more accurate sorting and grading of apples for firmness and SSC.

#### 4. Conclusion

In this research two hyperspectral imaging configurations (i.e., stationary and online) were tested for acquisition of spectral scattering images for three apple cultivars. Several methods, including discrete and continuous wavelet transform and conventional image texture analysis, were used to extract spectral and image characteristics for prediction of fruit firmness and SSC. Results showed that combinations of 1-D profile and 2-D image features were more effective than when they were used independently for evaluating the firmness and SSC. Good correlations were obtained for firmness for the three apple cultivars, using the features extracted by multi-scale techniques (i.e. *pCWT*, *iDWT*, and *iCWT*). Compared with the mean spectral scattering profile method (*pMeR*), the prediction models integrating both spectral and image features significantly improved firmness and SSC prediction; the standard error of prediction for GD, JG, RD apples was reduced by 6.6, 16.1, 13.7% for firmness, and by 11.2, 2.8, and 3.0% for SSC, respectively. However, SSC predictions for the online sensing configuration were still poor. Since the best prediction models generally had large numbers of latent variables, further improvements in feature extraction methods and their integration are needed in order to have more robust prediction models for fruit firmness and SSC.

#### Acknowledgement

The authors appreciate Ms. Amber Jablonski for providing help and technical support to this research.

#### References

- Birth, G.S., 1976. How light interacts with foods. In: Gafney, J.J. (Ed.), *Quality Detection in Foods*. ASAE, St. Joseph, MI, pp. 6–11.
- Cernadas, E., Carrión, P., Rodríguez, P.G., Muriel, E., Antequera, T., 2005. Analyzing magnetic resonance images of Iberian pork loin to predict its sensorial characteristics. *Comput. Vis. Image Underst.* 98, 344–360.
- Cho, Y.J., Han, Y.J., 1999. Nondestructive characterization of apple firmness by quantitation of laser scatter. *J. Texture Stud.* 30, 625–638.
- Dougherty, G., Henebry, G.M., 2001. Fractal signature and lacunarity in the measurement of the texture of trabecular bone in clinical CT images. *Med. Eng. Phys.* 23, 369–380.
- Fardet, A., Baldwin, P.M., Bertrand, D., Bouchet, B., Gallant, D.J., Barry, J.L., 1998. Textural images analysis of pasta protein networks to determine influence of technological processes. *Cereal Chem.* 75, 699–704.
- Galloway, M.M., 1975. Texture analysis using grey level run lengths. *Comput. Graph. Image Process.* 4, 172–179.
- Geraets, W.G.M., Van der Stelt, P.F., 2000. Fractal properties of bone. *Dentomaxillofac. Radiol.* 29, 144–153.
- Haralick, R.M., Shanmugan, K., Dinstein, I., 1973. Textural features for image classification. *IEEE Trans. Syst. Man Cybernet.* 3, 610–621.
- Kingston, C.M., 1992. Maturity indices for apple and pear. In: Janick, J. (Ed.), *Horticultural Reviews*, vol. 3. John Wiley & Sons, Inc., New York, pp. 407–432.
- Kube, P., Pentland, A., 1988. On the imaging of fractal surfaces. *IEEE Trans. Pattern Anal. Mach. Intell.* 10, 704–707.
- Lammertyn, J., Nicolai, B., Ooms, K., De Smedt, V., De Baerdemaeker, J., 1998. Non-destructive measurement of acidity, soluble solids, and firmness of Jonagold apples using NIR-spectroscopy. *Trans. ASAE* 41, 1089–1094.
- Lu, R., 2003. *Imaging Spectroscopy for Assessing Internal Quality of Apple Fruit*. ASAE Paper No. 036012. ASAE, St. Joseph, MI.
- Lu, R., 2004. Multispectral imaging for predicting firmness and soluble solids content of apple fruit. *Postharvest Biol. Technol.* 31, 147–157.
- Lu, R., 2007. Nondestructive measurements of firmness and soluble solids content for apple fruit using hyperspectral scattering images. *Sens. Instrum. Food Qual. Saf.* 1, 19–27.
- Lu, R., Guyer, D.E., Beaudry, R.M., 2000. Determination of firmness and sugar content of apples using near-infrared diffuse reflectance. *J. Texture Stud.* 31, 615–630.
- Lu, R., Huang, M., Qin, J., 2009. Analysis of hyperspectral scattering characteristics for predicting apple fruit firmness and soluble solids content. *Proc. SPIE*, doi:10.1117/12.819287, 7315, 73150I.
- Lu, R., Peng, Y., 2006. Hyperspectral scattering for assessing peach fruit firmness. *Biosyst. Eng.* 93, 161–171.
- Lu, R., Peng, Y., 2007. Development of a multispectral imaging prototype for real-time detection of apple fruit firmness. *Opt. Eng.* 46, 123201.
- Mallat, S.G., 1999. *A Wavelet Tour of Signal Processing*, 2nd ed. Academic Press, New York.
- Mandelbrot, B.B., 1982. *The Fractal Geometry of Nature*. Freeman, San Francisco, CA.
- McGlone, V.A., Abe, H., Kawano, S., 1997. Kiwifruit firmness by near infrared light scattering. *J. Near Infrared Spectrosc.* 5, 83–89.
- Mendoza, F., Dejmeck, P., Aguilera, J.M., 2007. Color and texture image analysis in classification of commercial potato chips. *Food Res. Int.* 40, 1146–1154.
- Mendoza, F., Valous, N.A., Allen, P., Kenny, T.A., Ward, P., Sun, D.W., 2009. Analysis and classification of commercial ham slice images using directional fractal dimension features. *Meat Sci.* 81, 313–320.
- Peng, Y., Lu, R., 2005. Modeling multispectral scattering profiles for prediction of apple fruit firmness. *Trans. ASAE* 48, 235–242.
- Peng, Y., Lu, R., 2006. An LCTF-based multispectral imaging system for estimation of apple fruit firmness. Part 2: selection of optimal wavelengths and development of prediction models. *Trans. ASAE* 49, 269–275.
- Peng, Y., Lu, R., 2008. Analysis of spatially resolved hyperspectral scattering images for assessing apple fruit firmness and soluble solids content. *Postharvest Biol. Technol.* 48, 52–62.
- Piñuela, J.A., Andina, D., McInnes, K.J., Tarquis, A.M., 2007. Wavelet analysis in a structured clay soil using 2-D images. *Nonlinear Processes Geophys.* 14, 425–434.
- Qin, J., Lu, R., 2007. Measurement of the absorption and scattering properties of turbid liquid foods using hyperspectral imaging. *Appl. Spectrosc.* 61, 388–396.
- Qin, J., Lu, R., 2008. Measurement of the optical properties of fruits and vegetables using spatially resolved hyperspectral diffuse reflectance imaging technique. *Postharvest Biol. Technol.* 49, 355–365.
- Qin, J., Lu, R., Peng, Y., 2009. Prediction of apple internal quality using spectral absorption and scattering properties. *Trans. ASAE* 52, 499–507.
- Qing, Z., Ji, B., Zude, M., 2007. Predicting soluble solid content and firmness in apple fruit by means of laser light backscattering image analysis. *J. Food Eng.* 82, 58–67.
- Russ, J.C., 2005. *Image Analysis of Food Microstructure*. CRC Press, Florida, pp. 98–110.
- Tu, K., De Busscher, R., De Baerdemaeker, J., Schrevens, E., 1995. Using laser beam as light source to study tomato and apple quality non-Destructively. In: *Proc. of the Food Processing Automation IV Conference*, 3–5 November 1995, Chicago, IL, pp. 528–536.
- Valous, N.A., Mendoza, F., Sun, D.W., Allen, P., 2009. Texture appearance characterization of pre-sliced pork ham images using fractal metrics: Fourier analysis dimension and lacunarity. *Food Res. Int.* 42, 353–362.